







The STRong lensing Insights into the Dark Energy Survey (STRIDES) 2016 follow-up campaign – II. New quasar lenses from double component fitting

T. Anguita ^{1,2★}, P. L. Schechter,³ N. Kuropatkin,⁴ N. D. Morgan,⁵ F. Ostrovski,^{6,7} L. E. Abramson ⁸, A. Agnello,⁹ Y. Apostolovski,¹ C. D. Fassnacht,¹⁰ J. W. Hsueh,¹⁰ V. Motta,¹¹ K. Rojas,¹¹ C. E. Rusu,¹² T. Treu,⁸ P. Williams ⁸, M. Auger,⁶ E. Buckley-Geer,⁴ H. Lin,⁴ R. McMahon,⁶ T. M. C. Abbott,¹³ S. Allam,⁴ J. Annis,⁴ R. A. Bernstein,¹⁴ E. Bertin,^{15,16} D. Brooks,¹⁷ D. L. Burke,^{18,19} A. Carnero Rosell,^{20,21} M. Carrasco-Kind,^{22,23} J. Carretero,²⁴ C. E. Cunha,¹⁸ C. B. D’Andrea,²⁵ J. De Vicente,²⁶ D. L. DePoy,²⁷ S. Desai,²⁸ H. T. Diehl,⁴ P. Doel,¹⁷ B. Flaugher,⁴ J. García-Bellido,²⁹ D. W. Gerdes,^{30,31} D. Gruen ^{18,19}, R. A. Gruendl,^{22,23} J. Gschwend,^{20,21} W. G. Hartley,^{17,32} D. L. Hollowood,³³ K. Honscheid,^{34,35} D. J. James,³⁶ K. Kuehn,³⁷ M. Lima,^{20,38} M. A. G. Maia,^{20,21} R. Miquel,^{24,39} A. A. Plazas,⁴⁰ E. Sanchez,²⁶ V. Scarpine,⁴ M. Smith,⁴¹ M. Soares-Santos ⁴², F. Sobreira,^{20,43} E. Suchyta ⁴⁴, G. Tarle³¹ and A. R. Walker¹³

Affiliations are listed at the end of the paper

Accepted 2018 August 7. Received 2018 August 02; in original form 2018 May 24

ABSTRACT

We report upon the follow-up of 34 candidate lensed quasars found in the Dark Energy Survey using NTT EFOSC, Magellan-IMACS, KECK-ESI, and SOAR-SAMI. These candidates were selected by a combination of double component fitting, morphological assessment, and colour analysis. Most systems followed up are indeed composed of at least one quasar image and 13 with two or more quasar images: two lenses, four projected binaries, and seven nearly identical quasar pairs (NIQs). The two systems confirmed as genuine gravitationally lensed quasars are one quadruple at $z_s = 1.713$ and one double at $z_s = 1.515$. Lens modelling of these two systems reveals that both systems require very little contribution from the environment to reproduce the image configuration. Nevertheless, small flux anomalies can be observed in one of the images of the quad. Further observations of nine inconclusive systems (including seven NIQs) will allow to confirm (or not) their gravitational lens nature.

Key words: gravitational lensing: strong – techniques: image processing – surveys – quasars: general.

1 INTRODUCTION

The space and time distortion produced by a massive galaxy in close projection to the line of sight of a distant object may produce multiple images of the background source. While this was predicted/theorized by Einstein (1936) and Zwicky (1937), it took over four decades to discover the first lensed quasar (Walsh, Car-

swell & Weymann 1979). Gravitationally lensed quasar systems are exceptional astrophysical and cosmological laboratories (e.g. Courbin, Saha & Schechter 2002), and as such, have been sought after ever since.

Unfortunately, lensed quasars systems are very rare phenomena, since they require the chance alignment of a (rare) quasar with a (rare) foreground massive deflector. Their density on the sky is estimated to be a tenth per square degree or less, at the typical limit of present and upcoming surveys (Oguri & Marshall 2010). Thus,

* E-mail: tanguita@gmail.com

finding lensed quasars requires wide area data sets and advanced techniques to sift through the large number of potential contaminants and false positives (e.g. Browne et al. 2003; Oguri et al. 2006). Until now, of order a couple of hundred lensed quasars are known, including a couple of dozens of quadruply imaged systems, which are the most valuable for many applications owing to their high information content. Therefore, most applications of lensed quasars are limited by sample size.

The current generation of wide field imaging surveys provides an opportunity to dramatically expand the samples of known lens quasars and thus benefit all of their scientific applications. The STRong lensing Insights into the Dark Energy Survey (STRIDES; strides.astro.ucla.edu) collaboration (Agnello et al. 2015; Treu et al. 2018) was formed to find gravitationally lensed quasars in the Dark Energy Survey (Dark Energy Survey Collaboration 2016, henceforth DES) with three broad ultimate goals: analysis of the dark matter content of the lensing galaxies (e.g. Schechter et al. 2014), analysis of the structure of the lensed quasars (e.g. Anguita et al. 2008a), and measurement of a ‘local’ Hubble constant via time delays (e.g. Bonvin et al. 2017).

Different groups within the STRIDES collaboration adopted complementary approaches to identifying lensed quasar systems. In all but a few cases the DES data alone do not suffice to classify a system as a ‘secure’ lens and follow-up observations are needed. Treu et al. 2018 give an overview of the 2016 follow-up campaign and report on results from two of the identification techniques. Here, we report results from a third such technique. Ostrovski et al. (in preparation) report results from a fourth technique.

While all four techniques begin with the some kind of colour selection, in the present approach that criterion is very broad, including many hundreds of thousands of objects. The second step is the automated decomposition of the selected sources into pairs of objects, which are then evaluated on morphological and refined colour criteria to produce candidate lensed systems. Operationally, the method ultimately involved the excision and analysis of more than a million *grizY* cutouts to produce a list of objects for visual inspection and possible follow-up.

In Section 2, we discuss the selection process. In Section 3, we describe the follow-up spectroscopic and imaging observations. In Section 4, we discuss 2 systems that can securely be classified as lensed quasars and 23 systems that cannot. In Section 5, we discuss nine systems for which the observations are inconclusive, including seven nearly identical quasar pairs (NIQs).

For all sections, a flat cosmology with $\Omega_m = 0.3$ and $H_0 = 70 \text{ km s}^{-1} \text{ Mpc}^{-1}$ was assumed unless otherwise specified.

2 SAMPLE SELECTION

To select our sample, we began with the *WISE* (Wright et al. 2010) catalogue and extracted $12 \text{ arcsec} \times 12 \text{ arcsec}$ DES *grizY* cutouts for objects with $m_{4.5\mu\text{m}} < 14.45$ and $m_{3.6\mu\text{m}} - m_{4.5\mu\text{m}} > 0.7$ on the Vega system. Stern et al. (2012) have shown that colour selection produces a sample of quasars of relatively high completeness and high purity. The low resolution of the *WISE* survey constitutes a virtue for our purposes: it ensures that the photometry does not suffer from partial resolution of the multiple lensed quasar images, which are typically separated by less than 2 arcsec . As such, close separation systems are identified as single objects and magnitude errors that arise from systems in close proximity, which are not deblended and treated separately, are avoided.

Rather than excise cutouts from the co-added DES images, we used the single best image in each filter as gauged by the effective

exposure time t_{eff} (see Table 1). t_{eff} is the ratio between the actual exposure time and the exposure time necessary to achieve the same signal to noise for point sources in nominal conditions (Morgan et al. 2018). To test if the object was indeed a multicomponent source, it was then split into two components as described by Schechter et al. (2017). Magnitudes were obtained for the two components by forcing the same splitting on all filters, taking the two components to have a common quasi-Gaussian surface brightness profile but deriving it from the pair itself, rather than using the local PSF as determined by the DES pipeline. If the quasi-Gaussian is substantially larger than the local Point Spread Function (PSF), the split object is rejected as a pair of galaxies.

When the signal-to-noise permitted, a second test was applied, using separate quasi-Gaussians for each component. If area inside half maximum of the quasi-Gaussians was more than two pixels greater than that of the local PSF in each of three filters, the pair was rejected. These two morphological rejection criteria run the risk of rejecting systems in which the light for the lensing galaxy makes a significant contribution. It was also found to fail for roughly 20 per cent of the known quasars in the analysed footprints, with two or three images being treated as a single extended image. This shortcoming was subsequently addressed by splitting objects into triplets when possible.

For the surviving pairs, a linear fit was obtained for the flux ratios (expressed in magnitudes) as a function of $\log \lambda$. As described by Schechter et al. (2017) they were given scores based on the slope of the fit and the scatter about the fit (hereafter, *ufom*). The highest scores were given to systems with small scatter and a slight slope in the flux ratio, favouring systems in which the fainter component is redder. Systems with scores less than 0.3 were not carried forward.

Combined magnitudes were computed by adding the fluxes of the two components using the calibration parameters produced by the DES pipeline; these were embedded in the fits headers. The *griz* colour combinations from these total magnitudes were then analysed using a Gaussian mixture model similar to that used by Ostrovski et al. (2017). Each pair was assigned relative probabilities $p(s)$, $p(g)$, and $p(q)$ of having star, galaxy, and quasar colours, respectively. Systems with $p(q) < 0.5$ were not carried forward (with a few exceptions as shown in Table 2).

The *grizY* cutouts for those systems with scores greater than 0.3 and $p(q) > 0.5$ were examined visually, as were all systems with scores greater than 0.5. Pairs were culled for a variety of somewhat subjective reasons. A final sample of 54 candidates resulted from the selection.

The DES cutouts were analysed in two groups, drawn, respectively, from the first and second year footprints of the DES (Flaugher 2005; Sánchez & DES Collaboration 2016). Note, however, that all imaging data used in this work resulted from the Y3A1 processing pipeline. The details of the DES imaging of the systems presented in this paper are shown in Table 1.

3 FOLLOW-UP

Thirty-four of the selected systems were followed up. Out of them, 32 spectroscopically. Twenty-two of them with NTT EFOSC2,¹ eight with ESI, and two with IMACS. Table 2 indicates the data obtained for each followed-up system. The details of each observing run are given in the 2016 STRIDES campaign overview paper (Treu et al. 2018), however, for completeness we describe them here as

¹PIDs 097.A-0473 and 098.A-0395, PI: ANGUIA.

Table 1. DES imaging data of the 34 lens candidate systems followed up. Exposure numbers, effective exposure time (t_{eff}), and average FWHM are shown for each band. Naming of the systems reflects the coordinates of the brightest component. Note that the effective exposure time (t_{eff}) is the ratio between the actual exposure time of the image (90 s in the g , r , i , and z bands, and 45 s in the Y band) and the exposure time necessary to achieve the same signal to noise for point sources in nominal conditions.

ID	Exposure number					t_{eff}					FWHM				
	g	r	i	z	Y	g	r	i	z	Y	g	r	i	z	Y
DESJ004306.87–411032.6	241210	369439	372931	253452	384081	0.63	0.65	0.50	0.94	1.24	1.19	1.22	1.31	0.74	0.84
DESJ005301.91+002042.9	257490	377405	*	377746	238105	0.79	0.77	*	0.89	1.07	1.08	1.16	*	0.87	0.97
DESJ005817.07–612004.6	387027	499372	370289	382172	470190	0.98	1.22	0.93	0.86	1.02	0.97	0.97	0.92	0.65	0.86
DESJ012006.38–435440.8	242801	242802	242803	256707	256708	1.05	0.92	1.03	1.03	1.26	1.32	1.28	1.11	0.92	0.90
DESJ013733.00–022242.6	240771	490665	372593	488823	384051	0.70	0.88	1.00	1.06	1.45	1.17	0.98	0.82	0.92	0.76
DESJ021524.22–472845.2	261270	258908	257598	257597	253506	0.92	1.22	0.97	1.05	1.36	0.92	0.92	0.84	0.93	0.79
DESJ023004.58–070445.9	363888	363890	363891	151376	349419	1.06	1.13	1.56	0.95	1.23	0.94	1.16	1.10	0.95	0.97
DESJ024018.40–020850.2	232436	361677	363897	253437	253418	0.87	0.87	1.20	0.96	1.15	1.07	1.02	1.06	0.79	0.71
DESJ025357.76–050454.7	277299	361681	361682	253449	253450	0.69	1.08	1.78	1.00	1.28	1.11	1.14	1.06	0.91	0.76
DESJ032559.42–451820.9	269629	269980	268015	513378	513379	1.00	0.86	1.08	1.10	1.42	1.03	1.09	0.98	0.77	0.77
DESJ040235.79–152328.4	363934	363938	363939	360692	359745	1.07	1.16	1.50	1.32	1.25	0.97	1.13	1.08	1.04	0.74
DESJ040559.80–330851.4	511795	511794	511793	403055	403823	0.98	1.27	1.65	2.02	3.05	0.95	1.09	0.99	1.10	0.67
DESJ040710.22–500600.9	268872	268873	257650	257651	266988	1.17	1.34	1.19	1.78	1.33	0.97	1.10	0.79	0.78	0.75
DESJ042553.23–453935.3	167349	167350	269672	263618	266247	1.11	1.15	1.24	1.00	1.12	1.03	1.02	0.92	0.89	0.78
DESJ043857.14–341609.9	402697	402339	403095	395561	386819	0.73	0.88	2.03	1.02	1.75	1.32	1.14	0.91	0.99	0.89
DESJ044042.84–200818.8	502762	502761	363955	403845	497417	1.07	1.18	1.43	1.15	1.58	1.00	0.96	0.98	0.84	0.81
DESJ044316.64–330845.1	500877	403096	403098	386431	386432	0.99	1.44	1.66	1.07	1.50	1.09	0.89	0.92	0.83	0.78
DESJ044402.20–371831.7	401196	381959	401938	386434	283819	1.33	0.92	1.67	1.05	0.91	0.93	1.08	0.82	0.87	0.77
DESJ045137.23–341006.0	500537	403101	402341	386820	395564	1.68	1.27	1.32	1.53	1.45	0.73	0.95	1.16	0.87	0.89
DESJ050912.77–235049.3	403481	500531	407990	404804	403873	0.89	2.84	1.34	0.85	1.47	1.05	0.82	0.83	0.92	0.77
DESJ051656.90–602031.4	270361	270364	270365	181024	405234	0.97	1.03	1.13	0.85	1.51	1.06	0.92	0.89	0.87	0.67
DESJ054430.63–592238.7	269310	515751	179958	267039	267040	0.73	0.88	0.52	0.78	1.12	1.12	0.98	1.02	0.84	0.82
DESJ060003.77–284758.5	271655	389583	390625	497865	408766	1.12	1.18	1.12	1.02	0.97	0.90	1.00	0.99	0.76	0.89
DESJ204726.90–480147.9	360503	367449	239553	487035	244132	0.65	0.61	0.80	0.53	1.06	1.25	1.21	0.90	0.97	0.82
DESJ210358.13–580049.0	230032	231072	231073	242675	479334	0.88	1.30	1.49	1.31	0.90	1.20	0.81	0.78	0.74	1.04
DESJ214148.85–462945.7	367473	371363	362359	364190	364625	0.65	0.91	2.07	0.81	1.13	1.24	0.86	0.74	0.82	0.93
DESJ215426.50–441044.4	371369	362366	474260	372006	372060	0.94	1.52	1.44	2.11	1.50	0.83	0.97	0.90	0.66	0.88
DESJ220039.00–471900.0	370205	367478	482106	372053	244206	0.62	0.68	1.10	0.95	0.96	1.11	1.14	0.85	0.95	0.94
DESJ221710.62+013808.3	242443	242429	233497	233499	479364	0.56	0.85	0.81	1.05	0.69	1.16	0.93	1.04	1.01	1.21
DESJ225007.92–604723.1	350159	362394	370229	374815	374808	1.36	1.00	0.80	0.95	1.20	0.87	0.95	0.94	0.72	0.70
DESJ230329.90–484430.5	233587	362393	362392	243157	355343	0.95	1.82	2.62	1.29	1.34	1.15	0.93	0.94	0.86	0.92
DESJ230602.30–565755.5	231544	350166	239693	466778	348401	0.84	1.41	1.60	1.07	2.67	1.27	0.90	0.96	0.88	0.74
DESJ232625.74–480548.5	350889	267575	475865	470026	469536	1.12	0.90	1.18	2.05	1.94	1.19	1.10	1.13	0.90	1.00
DESJ233713.66+005610.8	232371	239622	239639	242741	238084	0.59	0.95	1.27	2.35	1.02	1.24	1.01	0.97	0.78	1.09

Note: (*) No i band available.

Table 2. The 34 lensed candidate systems followed up, split into ‘Conclusive’ and ‘Inconclusive’ (those whose nature has been confirmed and those that it has not) as well as their classification. The columns show respectively: Name (ID), g -band magnitude of the faintest image (g), separation between the two images of the system in arcseconds ($\Delta\theta$), magnitude difference between the faintest and brightest image, respectively (g_{dif}), uform score as described in the text (ufom), quasar colour probability as described in the text ($p(q)$), spectroscopic follow instrument (Spec.), imaging follow-up instrument (Ima.), and measured quasar redshift if available (redshift). Redshift uncertainties are $\sigma_z \lesssim 0.001$.

		ID	g	$\Delta\theta$ (arcsec)	g_{dif}	ufom	$p(q)$	Spec.	Ima.	Redshift
Conclusive	Lens	DESJ 0405–3308	22.25	–	–0.84	1.5	$4e-3^a$	IMACS	SAMI, IMACS	$z = 1.713$
		DESJ 0407–5006	19.63	1.69	–1.27	0.67	0.76	EFOSC2	IMACS	$z = 1.515$
	Proj. Bin.	DESJ 0215–4728	19.99	1.07	–1.16	0.43	0.60	EFOSC2		$z_1 = 1.692, z_2 = 0.467$
		DESJ 0240–0208	19.22	0.94	–0.48	0.3	0.72	ESI		$z_1 = 1.685, z_2 = 1.058$
		DESJ 0425–4539	20.73	1.90	–1.08	0.41	$2e-6^b$	EFOSC2		$z_1 = 1.020, z_2 = 0.913$
		DESJ 2303–4844	20.93	2.21	–1.52	0.34	0.95	EFOSC2		$z_1 = 2.020, z_2 = 1.164$
	QSO + Star	DESJ 0053+0020	18.78	1.12	–0.85	0.62	$-^c$	ESI		$z = 1.320$
		DESJ 0325–4518	21.14	2.13	–1.44	0.33	0.60	EFOSC2		$z = 0.695$
		DESJ 0516–6020	19.65	2.52	–1.21	0.67	0.97	EFOSC2		$z = 1.039$
		DESJ 2103–5800	20.08	2.15	–0.67	0.37	0.02^d	EFOSC2		$z = 0.905$
		DESJ 2154–4410	19.50	1.94	–1.84	0.51	0.73	EFOSC2		$z = 1.750$
		DESJ 2217+0138	20.93	1.84	–1.82	0.38	0.95	EFOSC2		$z = 1.693$
		DESJ 2306–5657	19.92	2.17	–1.74	0.35	0.87	EFOSC2		$z = 1.010$
	QSO + Gal.	DESJ 0043–4110	21.91	3.17	–1.81	0.53	0.91	EFOSC2		$z = 0.882$
		DESJ 0438–3416	20.77	2.09	–1.60	0.46	0.92	EFOSC2		$z = 1.097$
		DESJ 0444–3718	20.50	3.53	–2.08	0.39	0.77	EFOSC2		$z = 1.345$
		DESJ 2326–4805	20.94	1.84	–2.36	0.59	0.70	EFOSC2		$z = 1.364$
	Em. Gal.	DESJ 0137–0222	20.31	0.85	–0.27	0.39	0.52		SAMI	
		DESJ 0253–0504	20.59	0.95	–1.32	0.46	0.58	ESI		
		DESJ 0402–1523	20.23	1.87	–0.60	0.36	0.79	ESI		
		DESJ 0440–2008	19.23	1.49	–0.97	0.33	0.56	ESI		
		DESJ 0443–3308	19.58	0.91	–2.84	0.30	0.96		SAMI	
		DESJ 0451–3410	21.39	0.99	–1.90	0.34	0.94	EFOSC2		
		DESJ 0600–2847	20.97	0.98	–1.47	0.31	0.81	ESI		
		DESJ 2047–4801	20.14	3.70	–0.87	0.56	0.91	IMACS		
Inconclusive	NIQ	DESJ 0058–6120	20.10	3.03	–2.49	0.43	0.95	EFOSC2	SAMI	$z = 1.322$
		DESJ 0120–4354	19.97	0.84	–0.15	0.38	0.86	EFOSC2		$z = 1.910$
		DESJ 0544–5922	18.93	1.24	–0.15	0.41	0.93	EFOSC2	IMACS	$z = 1.319$
		DESJ 2141–4629	20.46	0.91	–0.54	$-^e$	0.55	IMACS	SAMI	$z = 1.762$
		DESJ 2200–4719	19.78	3.60	–2.09	0.53	0.94	EFOSC2		$z = 1.608$
		DESJ 2250–6047	21.02	2.02	–1.31	0.46	0.70	EFOSC2	SAMI	$z = 1.080$
		DESJ 2337+0056	20.39	1.35	–0.91	0.79	0.93	EFOSC2	IMACS	$z = 0.710$
	Other	DESJ 0230–0704	18.05	0.57	–0.70	0.37	0.67	ESI	SAMI	QSO $z = 2.01$ + point source
		DESJ 0509–2350	19.94	1.99	–2.16	0.38	0.75	ESI	SAMI	QSO $z = 2.08$ + point source

^aFlagged for observation due to quad nature, despite low $p(q)$.

^bFlagged for observation due to the strong photometric variability observed, despite low $p(q)$.

^cNo i band available, precluding a $p(q)$ measurement.

^dFlagged for observation due to fairly blue colour ($g-i = 0.18$), despite low $p(q)$.

^e g -band fitting failed due to large seeing so no ufom measurement available. g magnitude difference extrapolated from the r , i , and z magnitude differences.

well. Table 2 shows the selection and follow-up parameters of all systems.

Note that for all spectroscopic observations, the slit angle was not defined at the parallactic angle but by the angle defined between the multiple lensed point-like images. As such, significant slit losses are expected in the spectra. Nevertheless, the validity of the flux ratio between multiple images should hold. Due to the nature of the observations, extraction was performed with custom routines: two Gaussian profiles were fitted wavelength wise on the data iteratively until residuals were minimized.

In addition, higher resolution imaging (than that provided by DES) was obtained for 11 systems (two of them without spectroscopic follow-up). Eight were observed with the 4.1 m Southern Astrophysical Research Telescope (SOAR) SAMI instrument at Cerro Pachon with its adaptive optics (AO) system SAM (Tokovinin et al. 2016). Imaging was carried out in the redder SAMI bands to maximize AO correction and optimize the contrast between quasar and

deflector galaxy. The pixel scale was $0.09 \text{ arcsec pix}^{-1}$ (2×2 binning of $0.045 \text{ arcsec pix}^{-1}$ pixels) and the typical exposure time was $3 \times 180 \text{ s}$. Four systems were observed with Magellan IMACS in its imaging mode.

4 CONCLUSIVE SYSTEMS

Twenty-five systems have had their nature confirmed by our spectroscopic follow-up. A summary of their properties and follow-up data is shown in Table 2.

4.1 Lenses

Two systems have been confirmed as genuine gravitationally lensed quasars. These two systems, besides having identical spectra of the two components, show evidence of a galaxy between them after subtraction of the quasar images. However, no absorption lines are

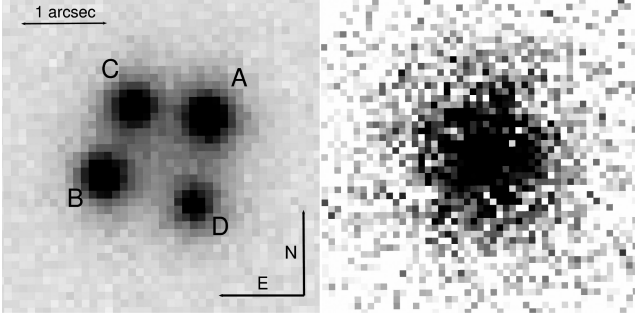


Figure 1. Left: DESJ 0405–3308 SOAR SAMI z image with naming convention. Right: Contrast enhanced ($10\times$) version of the same image with PSFs of the four quasar images subtracted.

Table 3. PSF fitting IMACS photometry (g , r , and i) SAMI (z) for the DES J0405–3308. The position of lensed quasar images was fixed to positions fitted with the high-resolution SAMI z image. Typical photometric uncertainty is 0.03 (mag).

Image	g	r	i	z
A	21.41	20.52	19.75	19.51
B	21.54	20.60	19.87	19.62
C	21.63	20.76	19.99	19.74
D	22.25	21.15	20.36	20.00
G	22.73	21.95	20.76	19.43

identified in the spectra of the systems, so no redshift measurement is available for their lensing galaxies. For these two systems we have performed PSF fitting to obtain the astrometry of the quasar images and lens galaxy in order to construct lens models. The PSF fitting was carried out using a purpose-built program that incorporates subroutines from the program DoPHOT (Schechter, Mateo & Saha 1993). It creates a tabulated PSF using a nearby star and simultaneously fits the tabulated PSF to the quasar images and a quasi-Gaussian to the central object. The lens models were performed using GLAFIC (Oguri 2010) and isothermal mass profiles.

4.1.1 DESJ 0405–3308

DESJ 0405–3308 follow-up imaging was obtained with Magellan IMACS in bands g , r , and i on 2016 November 29 and with SOAR SAMI in bands R , V , and z on 2016 December 3. The z -band image was used for PSF fitting astrometry measurements. The photometry for the lensed images and galaxy (see Fig. 1 for naming scheme) is shown in Table 3. A single slit was used on Magellan IMACS through images B and C. Fig. 2 shows the extracted spectra and the identified lines at a redshift of $z = 1.713 \pm 0.001$. The relative astrometry of the system is shown in Table 4.

In making the lens model, we have selected a singular isothermal ellipsoid (SIE) for the mass profile and have obtained a good fit within the astrometric uncertainties. The constraints used in the lens model are only the relative position of the quasar images and the lens galaxy. The best-fitting SIE parameters obtained were an Einstein radius $R_E = 0.69$ arcsec and an ellipticity $e = 0.17$ at a position angle $e_{PA} = 29^\circ$ (see Fig. 3). The secondary parameters obtained through the mass model are shown in Table 4. The small ellipticity result for the mass profile fit is consistent with the almost circular shape of the lensing galaxy. As such, no additional external perturbation (shear) was required for the model. We do note, however, that the range of allowed ellipticities for our lens model is $0.15 < e < 0.55$ at a

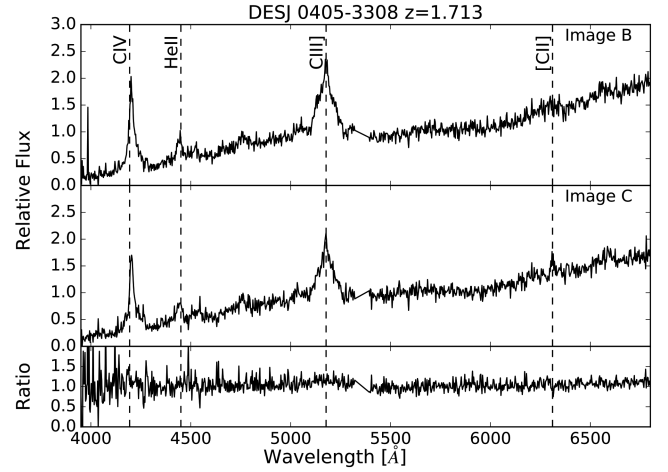


Figure 2. DESJ 0405–3308 Magellan IMACS spectra. Segmented lines show the identified emission lines used to measure the redshift shown above the figure panel. The lower panel shows the flux ratios between the quasar images.

90 per cent confidence level. Some rough consistency can be seen in the measured flux ratios (uncertainty smaller than 10 per cent) and the modelled flux ratios of images A and B, however, this is not the case with images C and D. In the case of image C, the almost negligible wavelength dependence of the observed flux ratios suggest that difference between the observed and modelled ratios might be due to substructure in the lens or environmental contributions, especially considering that no emission line residual is observed in the spectroscopic flux ratio between images C and B. In image D, the observed flux ratio increases by a factor 1.4 from the g to the z band. This chromatic variation could be explained by as well as differential dust extinction projected in front of image D (see e.g. Anguita et al. 2008b; Yonehara, Hirashita & Richter 2008). We note that both images C and D are saddle point images in the lens model and thus more prone to microlensing flux fluctuations (Schechter & Wambsganss 2002). Exploring these anomalies goes beyond the scope of this paper. Further space based and/or AO imaging along deeper spectroscopy will allow more detailed mass and flux models for the system.

4.1.2 DESJ 0407–5006

Follow-up imaging for DESJ 0407–5006 was obtained with Magellan IMACS in the i band on 2016 December 1. The photometry for the lensed images and galaxy is shown in Table 5 (see Fig. 4 for naming scheme). Follow-up spectra were obtained with NTT EFOSC2, as described above, with an exposure time of 600 s. Fig. 5 shows the extracted spectra and the identified emission lines at a redshift of $z = 1.515 \pm 0.001$. A slight emission line residual and chromaticity can be observed in the spectroscopic flux ratio. Although the significance of the signal does not allow us to draw any conclusions regarding microlensing in this system, it cannot be ruled out. Using the IMACS data and our PSF fitting technique we obtain the relative astrometry shown in Table 6.

The light profile fit shows a nearly circular shape for the lensing galaxy. Given the reduced number of positional constraints of this double system, we have selected a singular isothermal sphere plus external shear as a mass model and we have added the spectroscopic flux ratio measured on top of the CIII] and MgII emission lines as a constraint (we avoid using the CIV since it is very close to the edge of

Table 4. Observed and best-fitting modelled parameters for DESJ 0405–3308. Astrometry, flux ratios, and time delays with respect to image B. Since we do not have the redshift of the lensing galaxy, time delays are scaled such that $\Delta t = \Delta t^*(1 + z_l) \frac{D_L}{D_{LS}}$ days.

Comp	Astrometry			Flux ratios				Model output parameters						
	ΔRA	$\Delta Dec.$	Error	g	r	i	z	ΔRA	$\Delta Dec.$	κ	γ	μ	FR	
A	−1.211	0.674	0.040	1.13	1.08	1.12	1.11	−1.209	0.669	0.45	0.45	9.30	1.06	0.15
B	0.0	0.0	0.0	1.0	1.0	1.0	1.0	0.0	0.0	0.44	0.44	8.82	1.0	0.0
C	−0.349	0.819	0.050	0.92	0.86	0.90	0.90	−0.363	0.822	0.55	0.55	−9.27	1.05	1.02
D	−1.060	−0.311	0.070	0.52	0.60	0.64	0.71	−1.010	−0.343	0.58	0.58	−6.05	0.69	2.12
G	−0.680	0.216	0.120					−0.679	0.176					

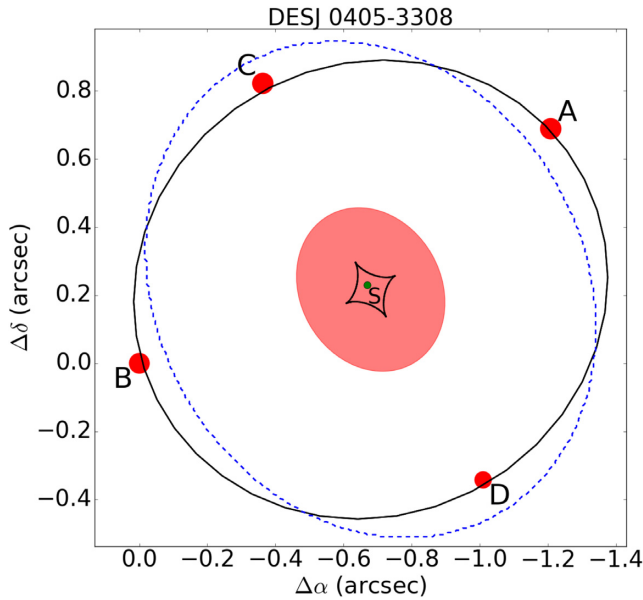
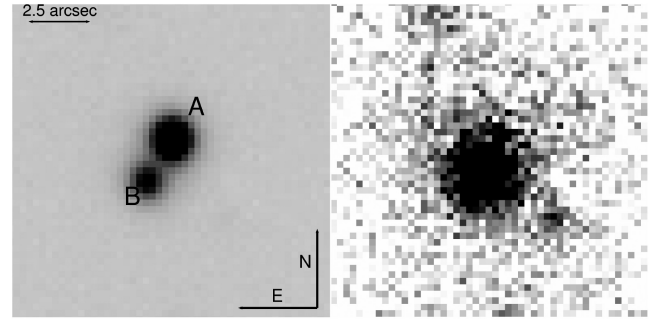
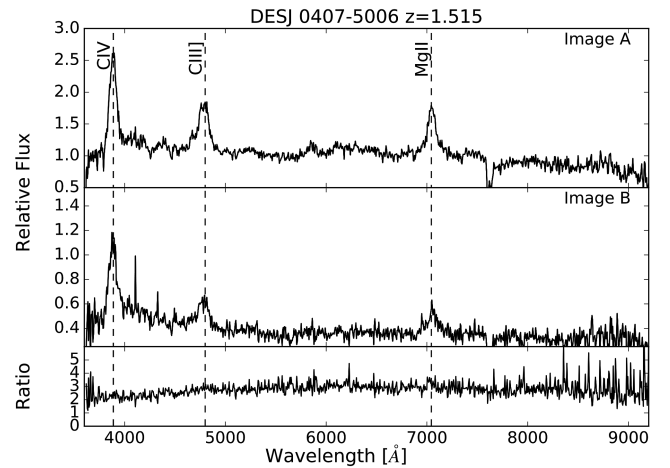
**Figure 3.** DESJ 0405–3308 lens model. Caustics are shown as solid lines and the critical curve as a segmented line. The source quasar and lensed images are labelled. The middle ellipse depicts the lensing galaxy.**Table 5.** Photometry for the DES J0407–5006. No galaxy was detected in the DES imaging so no photometry for the lensing galaxy is available. As the lensing galaxy was not fitted in the DES imaging, the flux of the lensed images is subject to contamination by it. Typical photometric uncertainties for Magellan and DES imaging are respectively 0.03 and 0.06 (mag).

Image	DES				IMACS
	g	r	i	z	i
A	18.35	18.07	18.00	18.10	18.01
B	19.62	19.36	19.19	19.19	19.26
G	–	–	–	–	19.97

the CCD) to the relative positions of the quasar images and the lens galaxy. We conservatively measure a flux ratio of $A/B = 3.0 \pm 0.2$, which is consistent with the observed i -band flux ratio. The best fit requires Einstein radius of $R_E = 0.87$ arcsec, together with a small external shear ($\gamma < 0.06$ at 90 per cent confidence) at 130 deg measured north to east (see Fig. 6). The secondary parameters obtained through the mass model are shown in Table 6. We note that due to the very small shear, even when the best-fitting position angle is at 130 deg east from north, the allowed range for this direction is poorly constrained to ± 45 deg. As with DESJ 0405–3308, further

**Figure 4.** Left: DESJ 0407–5006 Magellan IMACS i image with the naming convention. Right: Contrast enhanced ($30\times$) version of the same image with PSFs of the two quasar images subtracted.**Figure 5.** DESJ 0407–5006 NTT EFOSC2 spectra. Segmented lines show the identified emission lines used to measure the redshift shown above the figure panel. The lower panel shows the flux ratios between the quasar images.

space based and/or AO imaging along with deeper spectroscopy will allow more detailed mass and flux models of the system.

4.2 Contaminants

Several interlopers have been identified from our spectroscopic follow-up. These are all listed in Table 2. In particular, four projected double quasars are identified. Their spectra with line identification are shown in Fig. 7. Most of the confirmed contaminants (15) include at least one quasar (4 quasar pairs, 4 quasar–galaxy pairs, and 7 quasar–star pairs), with the 8 remaining being galaxies: 6 with

Table 6. Observed and best-fitting modelled parameters for DESJ 0407–5006. Astrometry, flux ratios, and time delays with respect to image B. Since we do not have the redshift of the lensing galaxy, time delays are scaled such that $\Delta t = \Delta t^*(1 + z_l) \frac{D_L}{D_{LS}}$ days.

Component	Astrometry			Flux ratio	Model output parameters						
	ΔRA	$\Delta Dec.$	Error	i	ΔRA	$\Delta Dec.$	κ	γ	μ	FR	
A	−0.863	1.437	0.002	3.17	−0.862	1.437	0.38	0.40	4.48	3.00	−25.46
B	0.0	0.0	0.004	1.0	0.0	0.0	0.81	0.84	−1.50	1.00	0.0
G	−0.331	0.424	0.06		−0.331	0.424					

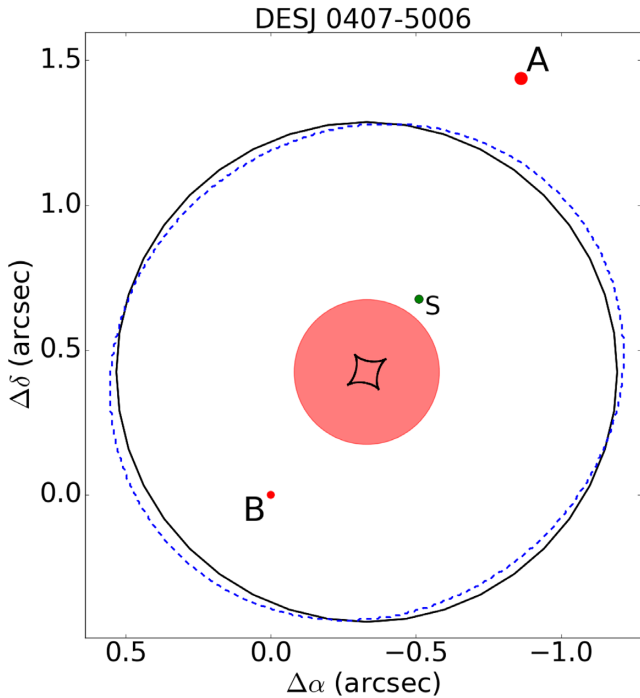


Figure 6. DESJ 0407–5006 lens model. Caustics are shown as solid lines and the critical curve as a segmented line. The source quasar and lensed images are labelled. The central ellipse depicts the lens galaxy.

measured strong narrow emission lines and 2 due to their extended shape from high-resolution SOAR SAMI imaging.

5 INCONCLUSIVE SYSTEMS

Despite the follow-up campaign, the nature of 9 out of the 34 systems still remains inconclusive. However, two subcategories of inconclusive systems are identified. A summary of their properties and follow-up data is shown in Table 2.

5.1 Nearly identical quasar pairs

NIQs are the systems followed up where we have obtained two resolved nearly identical quasar spectra of candidates, but we have not been able to identify a lensing galaxy in imaging. Seven of the systems in our follow-up sample are classified as NIQs. Most of these systems should be considered as very likely lensed quasars but we currently lack the imaging and/or spectroscopic observations to confirm them as such. The spectra of the image pairs in this category are shown in Fig. 8. Table 7 shows a crude estimation of the minimum brightness of the unidentified lens galaxy between the candidate lensed images using the image separation and source

redshift (see description of the method in Treu et al. 2018). Even though this is only an estimation, we note that several lens galaxies should have been bright enough for detection in the survey imaging ($i < 21.0$). Furthermore, out of the seven systems in the NIQ category, two show spectroscopic evidence supporting the interpretation of two different quasars at identical redshifts (i.e. physical binaries) as discussed below. However, conservatively and due to lack of evidence we still classify them as nearly identical pairs.

5.1.1 DESJ 0120–4354

This system at $z \approx 1.91$ shows a very broad double absorption blueward of the CIV line. At first sight this might be attributable to a lower redshift intervening system in between the two quasar images. However, the strength and broadness of the lines is not consistent with any known doublets. Another explored possibility was that they are two strong intervening MgII systems, however due to the small separation of the two quasar images (0.84 arcsec) these systems would appear in quasar image B. Furthermore, the profile of the SiIV+OIV lines shows a difference that could not be attributed to microlensing (see e.g. Sluse et al. 2012). Finally, image B shows a slightly lower redshift at $z = 1.909$ (versus image A at $z = 1.911$). As such, both quasar images could indeed be different systems, one of them a double BAL (Korista et al. 1993). This system has also been independently discovered by Ostrovski et al. (in preparation).

5.1.2 DESJ 2141–4629

Close inspection of the CIV emission line reveals very strong differences. In particular, the peak of the CIV emission in each image is red- and blueshifted, respectively. Furthermore, each peak coincides with an absorption in the other (see e.g. Hennawi et al. 2006). Two absorption systems have been identified at $z = 0.711$ and $z = 1.420$ from FeII triplet ($\sim 2370 \text{ \AA}$), FeII doublet ($\sim 2600 \text{ \AA}$), and MgII doublet ($\sim 2800 \text{ \AA}$) absorption. Given our current interpretation of the quasar spectra along the fact that the absorption lines resulting from these systems are too narrow to be due to a massive galaxy, we do not believe these are indicative of a lensing galaxy (see e.g. the discussion of broadness of absorption lines due to intervening systems in lensed quasars in Auger et al. 2008).

5.2 Otherwise inconclusive

Two additional systems followed up contain at least one image that has been confirmed to have a quasar spectrum. The spectroscopic flux obtained for the fainter image does not allow to identify its nature and as such also remain inconclusive.

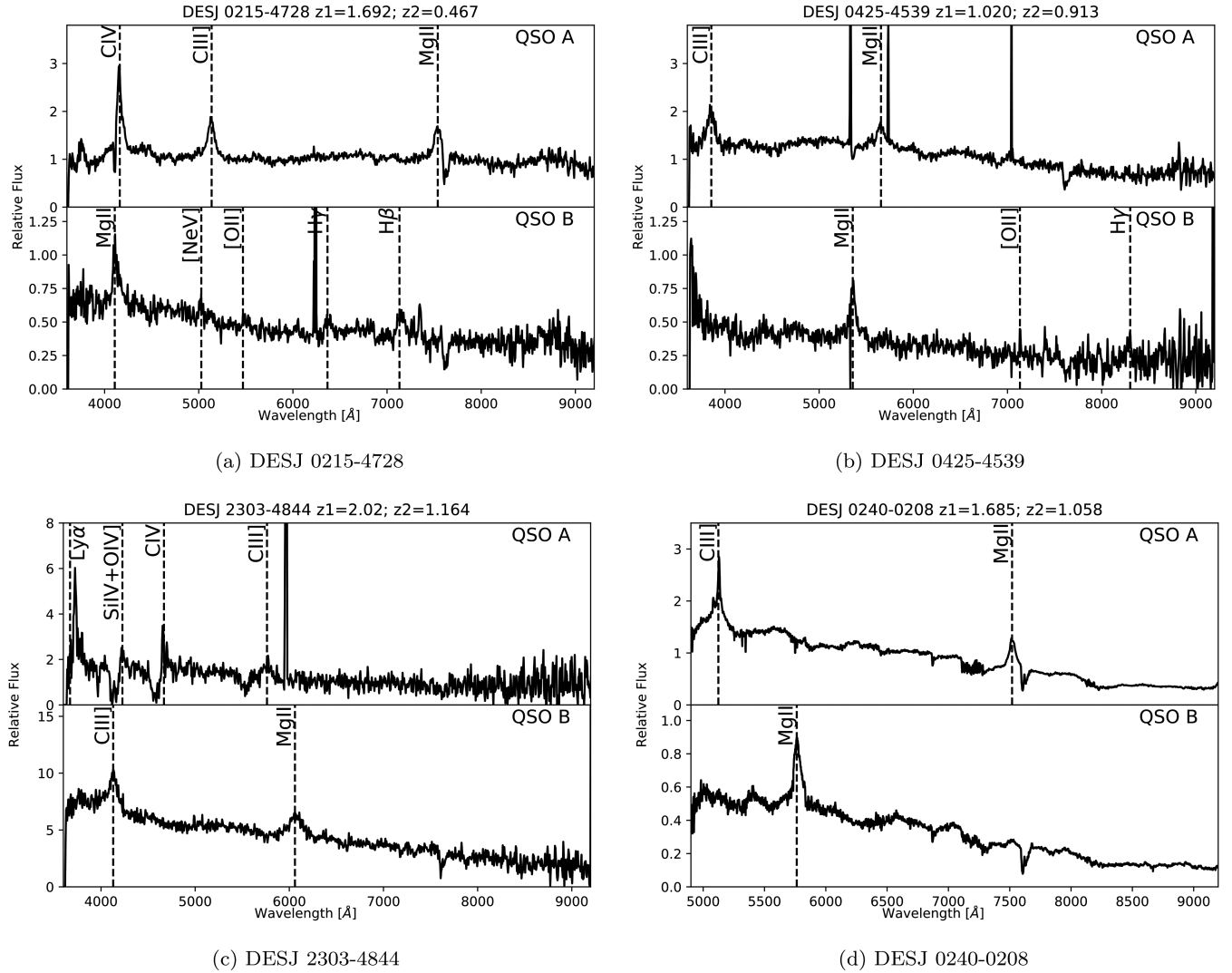


Figure 7. Projected binaries spectra. Segmented lines show the identified emission lines used to measure the redshifts shown above each panel.

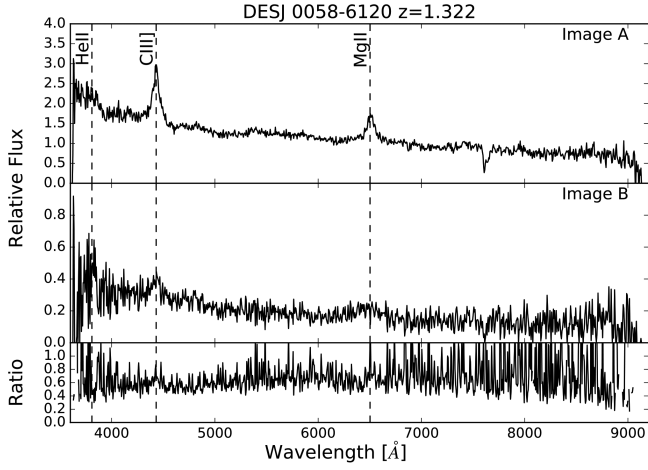
6 SUMMARY AND CONCLUSIONS

We have followed up 34 lensed quasar candidate systems selected by a mixture of multiband PSF fitting and colour selection in the fields of the DES. From this follow-up, two systems have conclusively been classified as gravitationally lensed quasars (one quadrupole and one double). Seven systems are likely double lensed quasars based on almost indistinguishable spectra between the two candidate images, but a hitherto unidentified lensing galaxy between them (NIQs). Two systems remain inconclusive since only one spectrum of the pairs is identified as a quasar. The remaining 23 systems have been confirmed as non-lensed systems (15 are indeed quasars with non-identical companions and 8 are pairs of compact low-redshift emission regions). Thus, removing the two completely inconclusive systems, we see our selection has an effectiveness of 30 per cent selecting identical pairs of quasars, or 50 per cent considering pairs of quasars (since 4 of the non-lensed systems are projected double quasar systems).

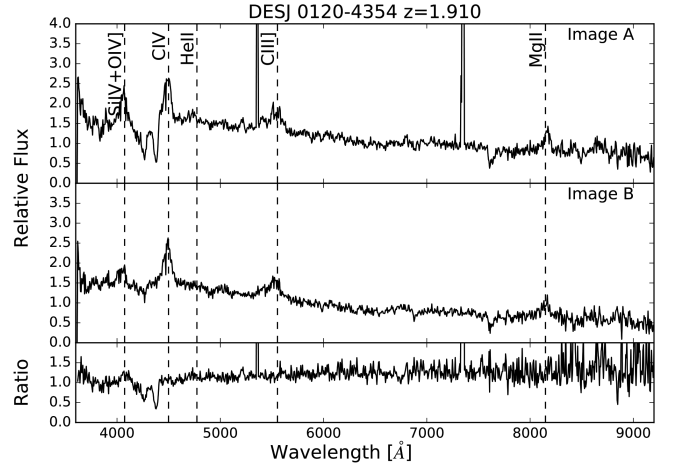
The two lensed quasar systems have been identified, thanks to deeper higher resolution images where a lensing galaxy could

be clearly identified, even when no absorption lines from them have been identified in the spectra. Deeper and higher resolution spectroscopy will allow us to measure their redshifts. Nevertheless, simple lens models were performed for both systems, and they reveal that a very minor quadrupole (internal or external) is required in order to reproduce the positional constraints, consistent with the observed light profile of the lensing galaxy. For the quadruply imaged quasar DES J0405–3308 two images show mild flux ratio inconsistencies with respect to the lens model, which could be consistent with microlensing or dust extinction from the lens galaxy. The same is true to an event lesser extent for DES J0407–5006.

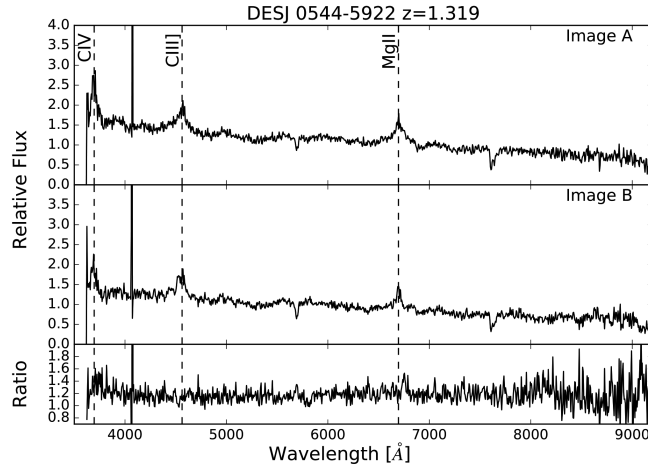
We have estimated the minimum brightness in the *griz* SDSS photometric bands for the possible lensing galaxy in the seven NIQs. Our estimations show that, if indeed lensed quasars, at least three of them should have been detected in the survey imaging image subtraction ($i < 21.0$). As such, priorities for follow-up should include a prior on image separation (larger separations imply brighter lenses, and thus lower probability of being lensed quasars if not detected in the survey imaging). We do note, however, that



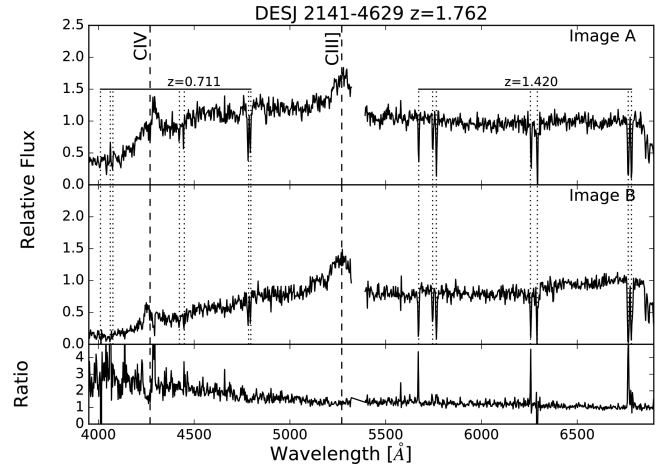
(a) DESJ 0058-6120



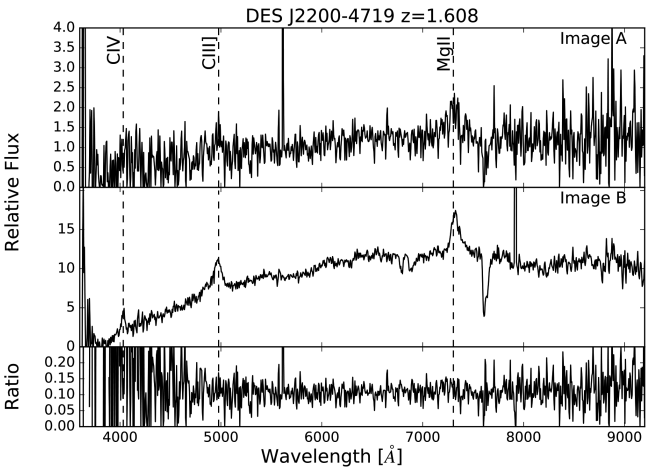
(b) DESJ 0120-4354



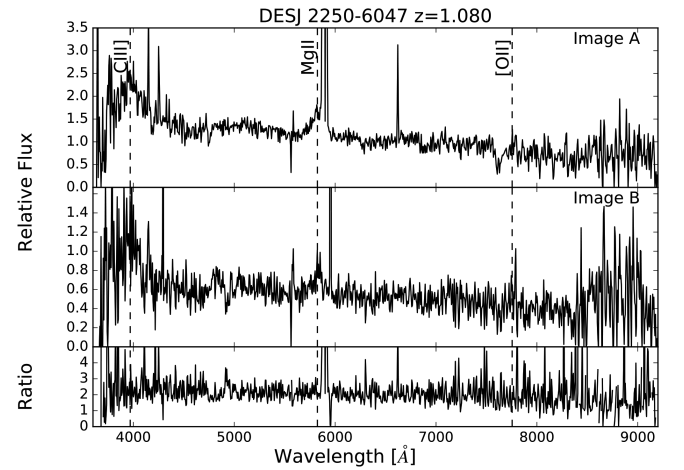
(c) DESJ 0544-5922



(d) DESJ 2141-4629

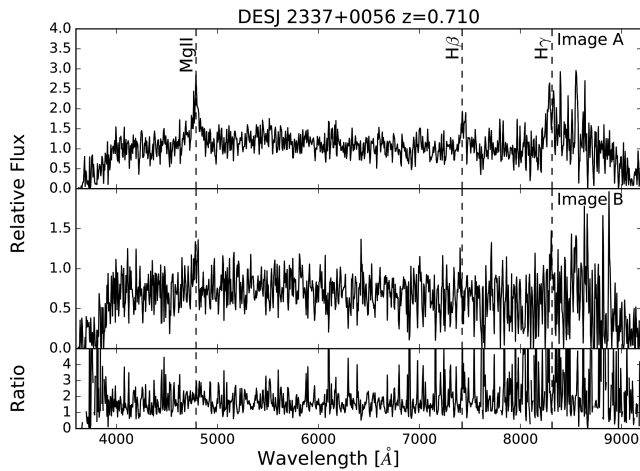


(e) DESJ 2200-4719



(f) DESJ 2250-6047

Figure 8. NIQs spectra. Segmented lines show the identified emission lines used to measure the redshifts shown above each panel. The lower panel shows the flux ratios between the quasar images.



(g) DESJ 2337+0056

Figure 8. *continued.*

Table 7. Maximum magnitude in the SDSS g , r , i , and z band for the possible lenses between the NIQs, obtained from the lensing mass expected due to the image separation of the candidate lensed images and their measured redshifts.

ID	g	r	i	z
DESJ 005817.0–612004	24.6	21.9	20.6	19.6
DESJ 012006.4–435441	28.7	26.2	24.6	23.3
DESJ 054430.6–592237	26.5	23.8	22.5	21.6
DESJ 214148.9–462946	25.9	23.1	21.8	20.5
DESJ 220039.1–471900	25.1	22.2	21.0	19.7
DESJ 225007.9–604724	24.3	22.1	20.7	20.2
DESJ 233713.7+005611	23.2	21.4	20.3	19.7

our magnitude estimates depend on several assumptions including lens redshifts. Furthermore, lens galaxies could well be hiding under the PSF wings of the, sometimes, much brighter quasar images, rendering the nominal depth optimistic. None the less, some of these systems are still worthy of follow-up to confirm their nature.

ACKNOWLEDGEMENTS

TA acknowledges support by proyecto FONDECYT 11130630 and by the Ministry for the Economy, Development, and Tourism's Programa Inicativa Científica Milenio through grant IC 12009, awarded to The Millennium Institute of Astrophysics (MAS). TT and VM acknowledge support by the Packard Foundation through a Packard Research Fellowship to TT. TT acknowledges support by the National Science Foundation through grant AST-1450141. CDF acknowledges support from the National Science Foundation through grant no. AST-1715611.

Funding for the DES Projects has been provided by the U.S. Department of Energy, the U.S. National Science Foundation, the Ministry of Science and Education of Spain, the Science and Technology Facilities Council of the United Kingdom, the Higher Education Funding Council for England, the National Center for Supercomputing Applications at the University of Illinois at Urbana-

Champaign, the Kavli Institute of Cosmological Physics at the University of Chicago, the Center for Cosmology and Astro-Particle Physics at the Ohio State University, the Mitchell Institute for Fundamental Physics and Astronomy at Texas A&M University, Financiadora de Estudos e Projetos, Fundação Carlos Chagas Filho de Amparo à Pesquisa do Estado do Rio de Janeiro, Conselho Nacional de Desenvolvimento Científico e Tecnológico and the Ministério da Ciência, Tecnologia e Inovação, the Deutsche Forschungsgemeinschaft, and the Collaborating Institutions in the Dark Energy Survey.

The Collaborating Institutions are Argonne National Laboratory, the University of California at Santa Cruz, the University of Cambridge, Centro de Investigaciones Energéticas, Medioambientales y Tecnológicas-Madrid, the University of Chicago, University College London, the DES-Brazil Consortium, the University of Edinburgh, the Eidgenössische Technische Hochschule (ETH) Zürich, Fermi National Accelerator Laboratory, the University of Illinois at Urbana-Champaign, the Institut de Ciències de l'Espai (IEEC/CSIC), the Institut de Física d'Altes Energies, Lawrence Berkeley National Laboratory, the Ludwig-Maximilians Universität München and the associated Excellence Cluster Universe, the University of Michigan, the National Optical Astronomy Observatory, the University of Nottingham, The Ohio State University, the University of Pennsylvania, the University of Portsmouth, SLAC National Accelerator Laboratory, Stanford University, the University of Sussex, Texas A&M University, and the OzDES Membership Consortium.

Based in part on observations at Cerro Tololo Inter-American Observatory, National Optical Astronomy Observatory, which is operated by the Association of Universities for Research in Astronomy (AURA) under a cooperative agreement with the National Science Foundation.

The DES data management system is supported by the National Science Foundation under grant numbers AST-1138766 and AST-1536171. The DES participants from Spanish institutions are partially supported by MINECO under grants AYA2015-71825, ESP2015-88861, FPA2015-68048, SEV-2012-0234, SEV-2016-0597, and MDM-2015-0509, some of which include ERDF funds from the European Union. IFAE is partially funded by the CERCA program of the Generalitat de Catalunya. Research leading to these results has received funding from the European Research Council under the European Union's Seventh Framework Program (FP7/2007-2013) including ERC grant agreements 240672, 291329, and 306478. We acknowledge support from the Australian Research Council Centre of Excellence for All-sky Astrophysics (CAASTRO), through project number CE110001020.

This manuscript has been authored by Fermi Research Alliance, LLC under Contract No. DE-AC02-07CH11359 with the U.S. Department of Energy, Office of Science, Office of High Energy Physics. The United States Government retains and the publisher, by accepting the article for publication, acknowledges that the United States Government retains a non-exclusive, paid-up, irrevocable, world-wide license to publish or reproduce the published form of this manuscript, or allow others to do so, for United States Government purposes.

(Some of) The data presented herein were obtained at the W. M. Keck Observatory, which is operated as a scientific partnership among the California Institute of Technology, the University of California and the National Aeronautics and Space Administration. The Observatory was made possible by the generous financial support of the W. M. Keck Foundation. The authors wish to recognize and acknowledge the very significant cultural role and reverence that the

summit of Maunakea has always had within the indigenous Hawaiian community. We are most fortunate to have the opportunity to conduct observations from this mountain. Based in part on observations obtained at the SOAR Telescope, which is a joint project of the Ministério da Ciência, Tecnologia, Inovações e Comunicações (MCTIC) do Brasil, the U.S. National Optical Astronomy Observatory (NOAO), the University of North Carolina at Chapel Hill (UNC), and Michigan State University (MSU). Based in part on observations made with ESO Telescopes at the La Silla Paranal Observatory. This publication makes use of data products from the *Wide-field Infrared Survey Explorer*, which is a joint project of the University of California, Los Angeles, and the Jet Propulsion Laboratory/California Institute of Technology, funded by the National Aeronautics and Space Administration. This publication includes data gathered with the 6.5 m Magellan Telescopes located at Las Campanas Observatory, Chile.

REFERENCES

- Agnello A. et al., 2015, *MNRAS*, 454, 1260
- Anguita T., Faure C., Yonehara A., Wambsganss J., Kneib J.-P., Covone G., Alloin D., 2008b, *A&A*, 481, 615
- Anguita T., Schmidt R. W., Turner E. L., Wambsganss J., Webster R. L., Loomis K. A., Long D., McMillan R., 2008a, *A&A*, 480, 327
- Auger M. W., Fassnacht C. D., Wong K. C., Thompson D., Matthews K., Soifer B. T., 2008, *ApJ*, 673, 778
- Bonvin V. et al., 2017, *MNRAS*, 465, 4914
- Browne I. W. A. et al., 2003, *MNRAS*, 341, 13
- Courbin F., Saha P., Schechter P. L., 2002, in Courbin F., Minniti D. eds, *Lecture Notes in Physics*, Vol. 608, *Gravitational Lensing: An Astrophysical Tool*. Springer Verlag, Berlin, p. 1
- Dark Energy Survey Collaboration, 2016, *MNRAS*, 460, 1270
- Einstein A., 1936, *Science*, 84, 506
- Flaugher B., 2005, *Int. J. Mod. Phys. A*, 20, 3121
- Hennawi J. F. et al., 2006, *AJ*, 131, 1
- Korista K. T., Voit G. M., Morris S. L., Weymann R. J., 1993, *ApJS*, 88, 357
- Morganson E. et al., 2018, *PASP*, 130, 074501
- Oguri M., 2010, *PASJ*, 62, 1017
- Oguri M., Marshall P. J., 2010, *MNRAS*, 405, 2579
- Oguri M. et al., 2006, *AJ*, 132, 999
- Ostrovski F. et al., 2017, *MNRAS*, 465, 4325
- Schechter P. L., Mateo M., Saha A., 1993, *PASP*, 105, 1342
- Schechter P. L., Morgan N. D., Chehade B., Metcalfe N., Shanks T., McDonald M., 2017, *AJ*, 153, 219
- Schechter P. L., Pooley D., Blackburne J. A., Wambsganss J., 2014, *ApJ*, 793, 96
- Schechter P. L., Wambsganss J., 2002, *ApJ*, 580, 685
- Sluse D., Hutsemékers D., Courbin F., Meylan G., Wambsganss J., 2012, *A&A*, 544, A62
- Stern D. et al., 2012, *ApJ*, 753, 30
- Sánchez E., DES Collaboration, 2016, *Nucl. Part. Phys. Proc.*, 273, 302
- Tokovinin A., Cantarutti R., Tighe R., Schurter P., Martinez M., Thomas S., van der Blik N., 2016, *PASP*, 128, 125003
- Treu T. et al. 2018, preprint ([arXiv:1808.04838](https://arxiv.org/abs/1808.04838))
- Walsh D., Carswell R. F., Weymann R. J., 1979, *Nature*, 279, 381
- Wright E. L. et al., 2010, *AJ*, 140, 1868
- Yonehara A., Hirashita H., Richter P., 2008, *A&A*, 478, 95
- Zwicky F., 1937, *ApJ*, 86, 217
- ²Millennium Institute of Astrophysics, Monseñor Nuncio Sotero Sanz 100, Oficina 104, 7500011 Providencia, Santiago, Chile
- ³MIT Kavli Institute for Astrophysics and Space Research, Cambridge, MA 02139, USA
- ⁴Fermi National Accelerator Laboratory, P. O. Box 500, Batavia, IL 60510, USA
- ⁵Staples High School, Westport, CT 06880, USA
- ⁶Institute of Astronomy, Madingley Road, Cambridge CB3 0HA, UK
- ⁷CAPES Foundation, Ministry of Education of Brazil, Brasília, DF 70040-020, Brazil
- ⁸Department of Physics and Astronomy, PAB, 430 Portola Plaza, Box 951547, Los Angeles, CA 90095-1547, USA
- ⁹European Southern Observatory, Karl-Schwarzschild-Strasse 2, D-85748 Garching bei München, DE, Germany
- ¹⁰Department of Physics, University of California Davis, 1 Shields Avenue, Davis, CA 95616, USA
- ¹¹Instituto de Física y Astronomía, Universidad de Valparaíso, Avda. Gran Bretaña 1111, Playa Ancha, Valparaíso 2360102, Chile
- ¹²Subaru Telescope, National Astronomical Observatory of Japan, 650 N Aohoku Pl, Hilo, HI 96720, USA
- ¹³Cerro Tololo Inter-American Observatory, National Optical Astronomy Observatory, Casilla 603, La Serena, Chile
- ¹⁴Observatories of the Carnegie Institution of Washington, 813 Santa Barbara St, Pasadena, CA 91101, USA
- ¹⁵CNRS, UMR 7095, Institut d'Astrophysique de Paris, F-75014 Paris, France
- ¹⁶Institut d'Astrophysique de Paris, Sorbonne Universités, UPMC Univ Paris 06, UMR 7095, F-75014 Paris, France
- ¹⁷Department of Physics & Astronomy, University College London, Gower Street, London WC1E 6BT, UK
- ¹⁸Kavli Institute for Particle Astrophysics & Cosmology, P. O. Box 2450, Stanford University, Stanford, CA 94305, USA
- ¹⁹SLAC National Accelerator Laboratory, Menlo Park, CA 94025, USA
- ²⁰Laboratório Interinstitucional de e-Astronomia – LIneA, Rua Gal. José Cristino 77, Rio de Janeiro, RJ 20921-400, Brazil
- ²¹Observatório Nacional, Rua Gal. José Cristino 77, Rio de Janeiro, RJ 20921-400, Brazil
- ²²Department of Astronomy, University of Illinois at Urbana-Champaign, 1002 W. Green Street, Urbana, IL 61801, USA
- ²³National Center for Supercomputing Applications, 1205 West Clark St., Urbana, IL 61801, USA
- ²⁴Institut de Física d'Altes Energies (IFAE), The Barcelona Institute of Science and Technology, Campus UAB, E-08193 Bellaterra (Barcelona), Spain
- ²⁵Department of Physics and Astronomy, University of Pennsylvania, Philadelphia, PA 19104, USA
- ²⁶Centro de Investigaciones Energéticas, Medioambientales y Tecnológicas (CIEMAT), 28040 Madrid, Spain
- ²⁷Department of Physics and Astronomy, George P. and Cynthia Woods Mitchell Institute for Fundamental Physics and Astronomy, Texas A&M University, College Station, TX 77843, USA
- ²⁸Department of Physics, IIT Hyderabad, Kandi, Telangana 502285, India
- ²⁹Instituto de Física Teórica UAM/CSIC, Universidad Autónoma de Madrid, E-28049 Madrid, Spain
- ³⁰Department of Astronomy, University of Michigan, Ann Arbor, MI 48109, USA
- ³¹Department of Physics, University of Michigan, Ann Arbor, MI 48109, USA
- ³²Department of Physics, ETH Zurich, Wolfgang-Pauli-Strasse 16, CH-8093 Zurich, Switzerland
- ³³Santa Cruz Institute for Particle Physics, Santa Cruz, CA 95064, USA
- ³⁴Center for Cosmology and Astro-Particle Physics, The Ohio State University, Columbus, OH 43210, USA
- ³⁵Department of Physics, The Ohio State University, Columbus, OH 43210, USA
- ³⁶Harvard-Smithsonian Center for Astrophysics, Cambridge, MA 02138, USA
- ³⁷Australian Astronomical Observatory, North Ryde, NSW 2113, Australia

¹Departamento de Ciencias Físicas, Universidad Andres Bello Fernandez Concha 700, 7591538 Las Condes, Santiago, Chile

³⁸*Departamento de Física Matemática, Instituto de Física, Universidade de São Paulo, CP 66318, São Paulo, SP 05314-970, Brazil*

³⁹*Institució Catalana de Recerca i Estudis Avançats, E-08010 Barcelona, Spain*

⁴⁰*Jet Propulsion Laboratory, California Institute of Technology, 4800 Oak Grove Dr., Pasadena, CA 91109, USA*

⁴¹*School of Physics and Astronomy, University of Southampton, Southampton SO17 1BJ, UK*

⁴²*Physics Department, Brandeis University, 415 South Street, Waltham, MA 02453, USA*

⁴³*Instituto de Física Gleb Wataghin, Universidade Estadual de Campinas, Campinas, SP 13083-859, Brazil*

⁴⁴*Computer Science and Mathematics Division, Oak Ridge National Laboratory, Oak Ridge, TN 37831, USA*

This paper has been typeset from a \TeX/L\AA\TeX file prepared by the author.